

## Error estimation for the automated multi-level substructuring method

Seung-Hwan Boo<sup>1</sup>, Jin-Gyun Kim<sup>2</sup> and Phill-Seung Lee<sup>1,\*</sup>,<sup>†</sup>

<sup>1</sup>*Department of Mechanical Engineering, Korea Advanced Institute of Science and Technology, 291 Daehak-ro, Yuseong-gu, Daejeon, 34141, Korea*

<sup>2</sup>*Mechanical Systems Safety Research Division, Korea Institute of Machinery and Materials, 156, Gajeongbuk-ro, Yuseong-gu, Daejeon, 34103, Korea*

### SUMMARY

In this study, we propose an effective method to estimate the reliability of finite element models reduced by the automated multi-level substructuring (AMLS) method. The proposed error estimation method can accurately predict relative eigenvalue errors in reduced finite element models. A new, enhanced transformation matrix for the AMLS method is derived from the original transformation matrix by properly considering the contribution of residual substructural modes. The enhanced transformation matrix is an important prerequisite to develop the error estimation method. Adopting the basic concept of the error estimation method recently developed for the Craig–Bampton method, an error estimation method is developed for the AMLS method. Through various numerical examples, we demonstrate the accuracy of the proposed error estimation method and explore its computational efficiency. Copyright © 2015 John Wiley & Sons, Ltd.

Received 22 May 2014; Revised 31 August 2015; Accepted 2 November 2015

**KEY WORDS:** structural dynamics; finite element method; component mode synthesis; automated multi-level substructuring; eigenvalue problem; error estimation

### 1. INTRODUCTION

These days, we frequently deal with finite element (FE) models with more than millions of degrees of freedom (DOFs) for analysis of ships, automobiles, and aircraft. Despite continuing advances in computing power, computational cost has continued to rise because of the rapidly increasing size of FE models used in engineering. For these reasons, it is crucial to reduce the computational time, and with that goal, various reduced-order modeling techniques have been developed since the 1960s [1–13].

Component mode synthesis (CMS) is one of the popular reduced-order modeling techniques (for example, references [6–12]) in structural dynamics. In CMS methods, an original (global) FE model is partitioned into several substructural models, substructural eigenvalue problems are solved, and a reduced FE model is constructed using dominant substructural modes. In this way, the large original FE model can be effectively approximated by a much smaller reduced model. CMS methods have been widely used to obtain effective reduced models for use in multi-body dynamics, structural health monitoring, structural design optimization, and real-time control of dynamic systems.

Since the 1990s, the automated multi-level substructuring (AMLS) method became popular because it offered great computational efficiency, along with recursive partitioning and matrix-reordering processes. The original idea of the AMLS method was developed in applied mathematics [14–17]. However, in the structural dynamics community, a well-defined formulation of the AMLS

\*Correspondence to: Phill-Seung Lee, Department of Mechanical Engineering, Korea Advanced Institute of Science and Technology, 291 Daehak-ro, Yuseong-gu, Daejeon, 34141, Korea.

<sup>†</sup>E-mail: phillseung@kaist.edu

method has recently been proposed that borrows from the basic concept of the Craig–Bampton (CB) method [7, 17].

Although various studies have been performed over the last several decades to improve CMS methods, several issues remain to be solved. One important issue is how to evaluate the reliability of reduced models. To handle this, various error estimation methods have been proposed [13, 18–21]. In general, relative eigenvalue errors are used for the reliability evaluation of reduced models. However, basically, it is difficult to estimate relative eigenvalue errors because the exact eigenvalues are unknown. Recently, a promising error estimation method was developed for the CB method [1]. The method provides accurate estimation of the relative eigenvalue errors in FE models reduced by the CB method.

The objective of this study is to develop an accurate error estimation method for the AMLS method. Because the AMLS method is based on the CB method [18], the concept of error estimation method developed for the CB method [1] can be also employed for the AMLS method. However, an important prerequisite is the need to obtain an enhanced transformation matrix for the AMLS method, based on consideration of the contribution of residual substructural modes. This is the major difficulty in development of the error estimation method for the AMLS method because of the relatively complicated architecture of the AMLS method. In this study, we derive the enhanced transformation matrix and using it, propose an error estimation method for the AMLS method. The proposed method presents excellent error estimation performance without heavy computation.

In the following sections, the original AMLS formulation is briefly reviewed, and the enhanced transformation matrix for the AMLS method is derived. We then propose an error estimation method for the AMLS method and evaluate the performance and computational efficiency of this new method through various numerical examples.

## 2. ORIGINAL FORMULATION OF THE AMLS METHOD

In structural dynamics, the free-vibration linear equations of motion for an undamped global (non-partitioned) structure can be expressed as

$$\mathbf{M}_g \ddot{\mathbf{u}}_g + \mathbf{K}_g \mathbf{u}_g = \mathbf{0}, \quad (1)$$

where  $\mathbf{M}_g$  and  $\mathbf{K}_g$  are the global mass and stiffness matrices, respectively, and  $\mathbf{u}_g$  is the global displacement vector. The subscript  $g$  denotes the global structure, and  $(\ddot{\phantom{x}}) = d^2(\phantom{x})/dt^2$ , where  $t$  is the time variable.

In CMS methods, the FE model of the global structure is partitioned into small substructural FE models as shown in Figure 1(a), and then various interface handling techniques are used. Because the AMLS method proposed by Bennighof [17, 23] is based on the CB method [7], the substructures are connected with a fixed interface boundary (Figure 1(b)).

In the AMLS method, interior DOFs are considered bottom-level substructures and interface DOFs are considered higher-level substructures, or the highest level substructure. The substructural relationship is defined using the terms ancestors and descendants. Higher-level substructures are

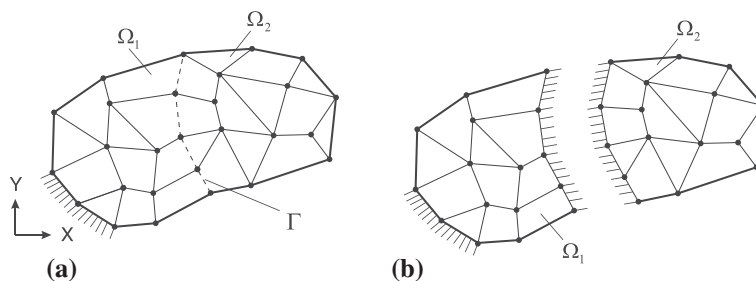


Figure 1. Partitioned structural model and interface handling in the automated multi-level substructuring method: (a) partitioned structure and (b) interface boundary treatment.



frequency  $\omega_i$  and that  $(\boldsymbol{\varphi}_g)_i$  is the corresponding mass normalized eigenvector. Those satisfy mass-orthonormality and stiffness-orthogonality conditions as follows:

$$(\boldsymbol{\varphi}_g)_i^T \mathbf{M}_g (\boldsymbol{\varphi}_g)_j = \delta_{ij} \text{ for } i, j = 1, 2, \dots, N_g, \tag{4a}$$

$$(\boldsymbol{\varphi}_g)_i^T \mathbf{K}_g (\boldsymbol{\varphi}_g)_j = \lambda_j \delta_{ij} \text{ for } i, j = 1, 2, \dots, N_g, \tag{4b}$$

where  $\delta_{ij}$  is the Kronecker delta ( $\delta_{ij} = 1$  if  $i = j$ , otherwise  $\delta_{ij} = 0$ ).

Using the eigenvectors obtained from Equation (3), the global displacement vector  $\mathbf{u}_g$  is defined as

$$\mathbf{u}_g = \boldsymbol{\Phi}_g \mathbf{q}_g, \tag{5}$$

where  $\boldsymbol{\Phi}_g$  is the global eigenvector matrix that contains all the eigenvectors  $(\boldsymbol{\varphi}_g)_i$  and  $\mathbf{q}_g$  is the corresponding generalized coordinate vector.

In the AMLS method, the global displacement vector  $\mathbf{u}_g$  is expressed by

$$\mathbf{u}_g = \mathbf{T}_0 \boldsymbol{\eta}_p \text{ with } \mathbf{T}_0 = \mathbf{T}^{(1)} \mathbf{T}^{(2)} \dots \mathbf{T}^{(N_s)} = \prod_{i=1}^{N_s} \mathbf{T}^{(i)}, \tag{6}$$

where the transformation matrix  $\mathbf{T}_0$  is given by sequentially multiplying the substructural transformation matrices  $\mathbf{T}^{(i)}$  from  $\mathbf{T}^{(1)}$  to  $\mathbf{T}^{(N_s)}$  and  $\boldsymbol{\eta}_p$  is the generalized coordinate vector for the partitioned structure. The subscript  $p$  denotes the partitioned structure.

Because of the recursive transformation procedure used in the AMLS method, the  $i^{\text{th}}$  incompletely transformed mass and stiffness matrices,  $\hat{\mathbf{M}}^{(i)}$  and  $\hat{\mathbf{K}}^{(i)}$ , are defined by

$$\begin{aligned} \hat{\mathbf{M}}^{(i)} &= \left( \mathbf{T}^{(1)} \mathbf{T}^{(2)} \dots \mathbf{T}^{(i)} \right)^T \mathbf{M}_g \left( \mathbf{T}^{(1)} \mathbf{T}^{(2)} \dots \mathbf{T}^{(i)} \right) \text{ and} \\ \hat{\mathbf{K}}^{(i)} &= \left( \mathbf{T}^{(1)} \mathbf{T}^{(2)} \dots \mathbf{T}^{(i)} \right)^T \mathbf{K}_g \left( \mathbf{T}^{(1)} \mathbf{T}^{(2)} \dots \mathbf{T}^{(i)} \right), \text{ for } i = 1, 2, \dots, (N_s - 1). \end{aligned} \tag{7}$$

In Equation (7), the  $i^{\text{th}}$  transformation matrix  $\mathbf{T}^{(i)}$  is given by

$$\mathbf{T}^{(i)} = \begin{bmatrix} \mathbf{I} & \mathbf{0} & & & \mathbf{0} \\ \mathbf{0} & \boldsymbol{\Phi}_i & \boldsymbol{\Psi}_{i,i+1} & \dots & \boldsymbol{\Psi}_{i,j} & \dots & \boldsymbol{\Psi}_{i,N_s} \\ \mathbf{0} & \mathbf{0} & & & \mathbf{I} & & \end{bmatrix}, \boldsymbol{\Phi}_i = \begin{bmatrix} \boldsymbol{\Phi}_i^d & \boldsymbol{\Phi}_i^r \end{bmatrix}, \tag{8}$$

$$\text{for } i = 1, 2, \dots, N_s, \quad j = i + 1, i + 2, \dots, N_s,$$

in which  $\boldsymbol{\Phi}_i$  and  $\boldsymbol{\Psi}_{i,j}$  are the eigenvector matrix of the  $i^{\text{th}}$  substructure and the constraint mode matrix to couple the  $i^{\text{th}}$  and  $j^{\text{th}}$  substructures, respectively. The eigenvector matrix  $\boldsymbol{\Phi}_i$  can be decomposed into the dominant term  $\boldsymbol{\Phi}_i^d$  and residual term  $\boldsymbol{\Phi}_i^r$ . The superscripts  $d$  and  $r$  denote the dominant and residual terms, respectively.

The eigenvector matrix  $\boldsymbol{\Phi}_i$  in Equation (8) is calculated from the following substructural eigenvalue problems

$$\hat{\mathbf{K}}_i^{(i-1)} \boldsymbol{\Phi}_i = \Lambda_i \hat{\mathbf{M}}_i^{(i-1)} \boldsymbol{\Phi}_i \text{ with } \hat{\mathbf{K}}_1^{(0)} = \mathbf{K}_1, \hat{\mathbf{M}}_1^{(0)} = \mathbf{M}_1 \text{ for } i = 1, 2, \dots, N_s, \tag{9}$$

where  $\Lambda_i$  is the eigenvalue matrix for the  $i^{\text{th}}$  substructure and  $\hat{\mathbf{M}}_i^{(i-1)}$  and  $\hat{\mathbf{K}}_i^{(i-1)}$  are the diagonal component mass and stiffness matrices of the  $i^{\text{th}}$  substructure in the  $(i - 1)^{\text{th}}$  incompletely transformed mass and stiffness matrices,  $\hat{\mathbf{M}}^{(i-1)}$  and  $\hat{\mathbf{K}}^{(i-1)}$ , defined in Equation (7). It is important to note that in order to obtain the  $i^{\text{th}}$  eigenvector matrix  $\boldsymbol{\Phi}_i$ , we use the  $(i - 1)^{\text{th}}$  incompletely transformed mass and stiffness matrices.



The global displacement vector in Equation 5 can be approximated as

$$\mathbf{u}_g \approx \bar{\mathbf{u}}_g = \bar{\Phi}_g \bar{\mathbf{q}}_g. \tag{17}$$

Comparing Equations (16) and (17), the following relations are obtained

$$\bar{\Phi}_g = \bar{\mathbf{T}}_0 \bar{\Phi}_p \text{ or } (\bar{\varphi}_g)_i = \bar{\mathbf{T}}_0 (\bar{\varphi}_p)_i. \tag{18}$$

In this paper, the original AMLS formulation is presented without any consideration of computational strategy. The formulation details of the multi-level computing strategy and the computational efficiency can be found elsewhere [17, 23, 24].

### 3. ENHANCED TRANSFORMATION MATRIX

As explained in the previous section, the reduced transformation matrix  $\bar{\mathbf{T}}_0$  is constructed retaining only the dominant substructural modes in the AMLS method. However, when the remaining residual substructural modes are considered, it is possible to enhance the reduced transformation matrix  $\bar{\mathbf{T}}_0$ . In order to derive the enhanced transformation matrix, it is necessary to decompose the original AMLS transformation matrix  $\mathbf{T}_0$  into dominant and residual parts.

After sequentially multiplying the substructural transformation matrices as in Equation (6), the obtained transformation matrix  $\mathbf{T}_0$  can be represented in terms of substructural component matrices as follows (for a detailed derivation, see Reference [24]),

$$\mathbf{T}_0 = \begin{bmatrix} \Phi_1 & & & & \\ & \ddots & & & \\ & & \Phi_i \hat{\Psi}_{i,j} \Phi_j & & \\ & & \mathbf{0} & \ddots & \\ & & & & \Phi_{N_s} \end{bmatrix} \text{ for } i = 1, 2, \dots, N_s, j = i + 1, i + 2, \dots, N_s. \tag{19}$$

The transformation matrix in Equation (19) is then decomposed into two parts

$$\mathbf{T}_0 = \hat{\Psi} \Phi \text{ with } \hat{\Psi} = \begin{bmatrix} \mathbf{I} & & & & \\ & \ddots & & & \\ & & \mathbf{I} \hat{\Psi}_{i,j} & & \\ & & \mathbf{0} & \ddots & \\ & & & & \mathbf{I} \end{bmatrix}, \Phi = \begin{bmatrix} \Phi_1 & & & & \\ & \ddots & & & \\ & & \Phi_i & & \mathbf{0} \\ & & \mathbf{0} & \ddots & \\ & & & & \Phi_{N_s} \end{bmatrix}, \tag{20}$$

where  $\hat{\Psi}$  is the multi-level constraint mode matrix,  $\hat{\Psi}_{i,j}$  are the substructural component matrices located in the upper triangular part of  $\hat{\Psi}$ , and  $\Phi$  is the eigenvector matrix that contains all the substructural eigenvector matrices. Note that in Equation (20),  $\hat{\Psi}$  and  $\Phi$  are  $N_g \times N_g$  matrices.

The multi-level constraint mode matrix  $\hat{\Psi}$  is obtained by sequentially multiplying the substructural constraint mode matrices  $\Psi^{(i)}$

$$\hat{\Psi} = \prod_{i=1}^{N_s-1} \Psi^{(i)} \text{ with } \Psi^{(i)} = \begin{bmatrix} \mathbf{I} & \mathbf{0} & & & \mathbf{0} \\ \mathbf{0} & \mathbf{I} & \Psi_{i,i+1} & \dots & \Psi_{i,j} & \dots & \Psi_{i,N_s} \\ \mathbf{0} & \mathbf{0} & & & \mathbf{I} & & \end{bmatrix}, \tag{21}$$

$$\text{for } i = 1, 2, \dots, (N_s - 1), j = i + 1, i + 2, \dots, N_s,$$

in which  $\Psi^{(i)}$  is  $N_g \times N_g$  matrix. Note that  $\Psi^{(i)}$  looks similar to  $\mathbf{T}^{(i)}$  in Equation (8), except for the identity matrix in its  $i^{\text{th}}$  diagonal component.



Note that Equation (26) presents the exact equations of motion that contain all the substructural modes. Using the second row in Equation (27), the following relation is obtained

$$\boldsymbol{\eta}_p^r = \lambda(\boldsymbol{\Lambda}_r - \lambda\mathbf{M}_{rr})^{-1}\mathbf{M}_{dr}^T\boldsymbol{\eta}_p^d. \tag{29}$$

Substituting Equation (29) into Equation (25), the global displacement vector  $\mathbf{u}_g$  is represented by

$$\mathbf{u}_g = \left[ \mathbf{T}_0^d + \lambda\mathbf{T}_0^r(\boldsymbol{\Lambda}_r - \lambda\mathbf{M}_{rr})^{-1}\mathbf{M}_{dr}^T \right] \boldsymbol{\eta}_p^d. \tag{30}$$

We use  $\mathbf{T}_0^r = \hat{\boldsymbol{\Psi}}\boldsymbol{\Phi}_r$  (in Equation (24)) and  $\mathbf{M}_{dr}$  (in Equation (28b)) in Equation (30), and obtain

$$\mathbf{u}_g = \mathbf{T}_0^d\boldsymbol{\eta}_p^d + \lambda\hat{\boldsymbol{\Psi}}\hat{\mathbf{F}}_r\hat{\boldsymbol{\Psi}}^T\mathbf{M}_g\mathbf{T}_0^d\boldsymbol{\eta}_p^d, \tag{31}$$

with

$$\hat{\mathbf{F}}_r = \boldsymbol{\Phi}_r(\boldsymbol{\Lambda}_r - \lambda\mathbf{M}_{rr})^{-1}\boldsymbol{\Phi}_r^T, \tag{32}$$

where  $\hat{\mathbf{F}}_r$  denotes the residual flexibility of substructures.

Using Taylor expansion, the residual flexibility matrix  $\hat{\mathbf{F}}_r$  can be rewritten as

$$\begin{aligned} \hat{\mathbf{F}}_r &= \boldsymbol{\Phi}_r(\boldsymbol{\Lambda}_r - \lambda\mathbf{M}_{rr})^{-1}\boldsymbol{\Phi}_r^T \\ &= \boldsymbol{\Phi}_r\boldsymbol{\Lambda}_r^{-1}\boldsymbol{\Phi}_r^T + \lambda\boldsymbol{\Lambda}_r^{-1}\mathbf{M}_{rr}\boldsymbol{\Lambda}_r^{-1}\boldsymbol{\Phi}_r^T + \mathcal{O}(\lambda^2) + \mathcal{O}(\lambda^3) + \dots \end{aligned} \tag{33}$$

Substituting Equation (33) into Equation (31) and truncating terms higher than order of  $\lambda$ , the global displacement vector  $\mathbf{u}_g$  is approximated by

$$\mathbf{u}_g \approx \bar{\mathbf{u}}_g = \bar{\mathbf{T}}_1\boldsymbol{\eta}_p^d, \quad \bar{\mathbf{T}}_1 = \bar{\mathbf{T}}_0 + \lambda\bar{\mathbf{T}}_r, \tag{34a}$$

$$\bar{\mathbf{T}}_0 = \mathbf{T}_0^d, \quad \bar{\mathbf{T}}_r = \hat{\boldsymbol{\Psi}}\mathbf{F}_{rs}\hat{\boldsymbol{\Psi}}^T\mathbf{M}_g\mathbf{T}_0^d, \quad \mathbf{F}_{rs} = \boldsymbol{\Phi}_r\boldsymbol{\Lambda}_r^{-1}\boldsymbol{\Phi}_r^T, \tag{34b}$$

where  $\bar{\mathbf{T}}_1$  is an enhanced transformation matrix and  $\mathbf{F}_{rs}$  is the 0<sup>th</sup>-order term of the residual flexibility  $\hat{\mathbf{F}}_r$ .

In Equation (34b),  $\mathbf{F}_{rs}$  can be indirectly calculated by subtracting the dominant flexibility from the full flexibility

$$\mathbf{F}_{rs} = \boldsymbol{\Phi}_r\boldsymbol{\Lambda}_r^{-1}\boldsymbol{\Phi}_r^T = \begin{bmatrix} \mathbf{F}_1^{rs} & & & & \\ & \ddots & & & \\ & & \mathbf{F}_i^{rs} & & \mathbf{0} \\ & & & \ddots & \\ \mathbf{0} & & & & \mathbf{F}_{N_s-1}^{rs} \\ & & & & & \mathbf{0} \end{bmatrix}, \tag{35}$$

$$\mathbf{F}_i^{rs} = \left(\hat{\mathbf{K}}_i^{(i-1)}\right)^{-1} - \left(\boldsymbol{\Phi}_i^d\right)\left(\boldsymbol{\Lambda}_i^d\right)^{-1}\left(\boldsymbol{\Phi}_i^d\right)^T \text{ for } i = 1, 2, \dots, (N_s - 1), \tag{36}$$

in which  $\left(\hat{\mathbf{K}}_i^{(i-1)}\right)^{-1}$  and  $\left(\boldsymbol{\Phi}_i^d\right)\left(\boldsymbol{\Lambda}_i^d\right)^{-1}\left(\boldsymbol{\Phi}_i^d\right)^T$  are the full and dominant flexibility matrices for the  $i^{\text{th}}$  substructure.

To construct the enhanced transformation matrix  $\bar{\mathbf{T}}_1$ ,  $\mathbf{F}_{rs}$  needs to be additionally calculated using Equations (35) and (36). However,  $\mathbf{F}_{rs}$  is simply calculated by reusing  $\left(\hat{\mathbf{K}}_i^{(i-1)}\right)^{-1}$ , already calculated in Equation (10), and the dominant substructural eigensolutions  $\boldsymbol{\Lambda}_i^d$  and  $\boldsymbol{\Phi}_i^d$ , already obtained from Equation (9). Therefore, not much additional cost for computation is required.

Using the enhanced transformation matrix  $\bar{\mathbf{T}}_1$ , the  $i^{\text{th}}$  approximated global eigenvector  $(\bar{\varphi}_g)_i$  is more accurately represented by

$$(\bar{\varphi}_g)_i = \bar{\mathbf{T}}_1(\bar{\varphi}_p)_i \text{ with } \bar{\mathbf{T}}_1 = \bar{\mathbf{T}}_0 + \lambda \bar{\mathbf{T}}_r. \tag{37}$$

Note that the enhanced transformation matrix  $\bar{\mathbf{T}}_1$  is more precise than the original transformation matrix  $\bar{\mathbf{T}}_0$ . Therefore,  $\bar{\mathbf{T}}_1$  could be adopted to improve the original AMLS method. However, in this case, the unknown eigenvector  $\lambda$  contained in  $\bar{\mathbf{T}}_1$  would need to be properly handled.

#### 4. ERROR ESTIMATION METHOD

In this section, we present an error estimation method to precisely evaluate the relative eigenvalue errors in the AMLS method when the exact global eigenvalues  $\lambda_i$  are unknown. The basic procedure is similar to the error estimation method recently developed for the CB method [22].

In CMS methods, the following relative eigenvalue error is generally used to evaluate the reliability of reduced FE models

$$\xi_i = \frac{\bar{\lambda}_i - \lambda_i}{\lambda_i} = \frac{\bar{\lambda}_i}{\lambda_i} - 1, \tag{38}$$

in which  $\xi_i$  denotes the relative eigenvalue error for the  $i^{\text{th}}$  mode and the exact global eigenvalue  $\lambda_i$  is obtained from the eigenvalue problem of the global FE model by solving Equation (3).

From the global eigenvalue problem in Equation (3), the following equation is given

$$\frac{1}{\lambda_i}(\varphi_g)_i^T \mathbf{K}_g(\varphi_g)_i = (\varphi_g)_i^T \mathbf{M}_g(\varphi_g)_i, \tag{39}$$

where the exact global eigensolutions  $\lambda_i$  and  $(\varphi_g)_i$  satisfy the mass-orthonormality and stiffness-orthogonality conditions.

Here, the exact global eigenvector  $(\varphi_g)_i$  in Equation (39) can be approximated using the enhanced transformation matrix  $\bar{\mathbf{T}}_1$  described in Equation (37)

$$(\varphi_g)_i \approx \bar{\mathbf{T}}_1(\bar{\varphi}_p)_i = [\bar{\mathbf{T}}_0 + \lambda_i \bar{\mathbf{T}}_r] (\bar{\varphi}_p)_i. \tag{40}$$

Using Equation (40) in Equation (39), the following equation is obtained

$$\frac{\bar{\lambda}_i}{\lambda_i} - 1 \approx (\bar{\varphi}_p)_i^T [2\lambda_i \bar{\mathbf{T}}_0^T \mathbf{M}_g \bar{\mathbf{T}}_r - 2\bar{\mathbf{T}}_0^T \mathbf{K}_g \bar{\mathbf{T}}_r - \lambda_i \bar{\mathbf{T}}_r^T \mathbf{K}_g \bar{\mathbf{T}}_r + \lambda_i^2 \bar{\mathbf{T}}_r^T \mathbf{M}_g \bar{\mathbf{T}}_r] (\bar{\varphi}_p)_i, \tag{41}$$

in which the left-hand side of Equation (41) is the relative eigenvalue error  $\xi_i$  (Equation (38)). This implies that the relative eigenvalue error can be calculated by the right-hand side of Equation (41). However, the right-hand side of Equation (41) contains unknowns  $\lambda_i$ , which must be properly handled first.

We assume that the approximated eigenvalue  $\bar{\lambda}_i$  is very close to the exact eigenvalue  $\lambda_i$  in Equation (41). We then use  $\bar{\lambda}_i$  instead of  $\lambda_i$ , and Equation (41) is approximated as

$$\xi_i \approx (\bar{\varphi}_p)_i^T [2\bar{\lambda}_i \bar{\mathbf{T}}_0^T \mathbf{M}_g \bar{\mathbf{T}}_r - 2\bar{\mathbf{T}}_0^T \mathbf{K}_g \bar{\mathbf{T}}_r - \bar{\lambda}_i \bar{\mathbf{T}}_r^T \mathbf{K}_g \bar{\mathbf{T}}_r + \bar{\lambda}_i^2 \bar{\mathbf{T}}_r^T \mathbf{M}_g \bar{\mathbf{T}}_r] (\bar{\varphi}_p)_i. \tag{42}$$

Using  $\mathbf{T}_0^d (= \bar{\mathbf{T}}_0)$  in Equation (24) and  $\bar{\mathbf{T}}_r$  in Equation (34b),  $\bar{\mathbf{T}}_0^T \mathbf{M}_g \bar{\mathbf{T}}_r$  and  $\bar{\mathbf{T}}_0^T \mathbf{K}_g \bar{\mathbf{T}}_r$  in Equation (42) are expressed as

$$\bar{\mathbf{T}}_0^T \mathbf{M}_g \bar{\mathbf{T}}_r = \Phi_d^T \tilde{\mathbf{M}}_g \mathbf{F}_{rs} \tilde{\mathbf{M}}_g \Phi_d \text{ with } \tilde{\mathbf{M}}_g = \hat{\Psi}^T \mathbf{M}_g \hat{\Psi}, \tag{43a}$$

$$\bar{\mathbf{T}}_0^T \mathbf{K}_g \bar{\mathbf{T}}_r = \Phi_d^T \tilde{\mathbf{K}}_g \mathbf{F}_{rs} \tilde{\mathbf{M}}_g \Phi_d \text{ with } \tilde{\mathbf{K}}_g = \hat{\Psi}^T \mathbf{K}_g \hat{\Psi}. \tag{43b}$$

In Equation (43b), it is identified that  $\Phi_d^T \tilde{\mathbf{K}}_g \mathbf{F}_{rs} = \mathbf{0}$  in  $\bar{\mathbf{T}}_0^T \mathbf{K}_g \bar{\mathbf{T}}_r$ , because  $\Phi_d^T$  and  $\mathbf{F}_{rs}$  have a orthogonality for the matrix  $\tilde{\mathbf{K}}_g$ . Thus, Equation (43b) becomes

$$\bar{\mathbf{T}}_0^T \mathbf{K}_g \bar{\mathbf{T}}_r = \mathbf{0}. \tag{44}$$

Substituting  $\bar{\mathbf{T}}_r$  in Equation (34b) into  $\bar{\mathbf{T}}_r^T \mathbf{K}_g \bar{\mathbf{T}}_r$  in Equation (42), the following equation is obtained

$$\bar{\mathbf{T}}_r^T \mathbf{K}_g \bar{\mathbf{T}}_r = \Phi_d^T \tilde{\mathbf{M}}_g \mathbf{F}_{rs} \tilde{\mathbf{K}}_g \mathbf{F}_{rs} \tilde{\mathbf{M}}_g \Phi_d, \tag{45}$$

and because  $\mathbf{F}_{rs} \tilde{\mathbf{K}}_g \mathbf{F}_{rs} = \mathbf{F}_{rs}$ , we have the following relation:

$$\bar{\mathbf{T}}_0^T \mathbf{M}_g \bar{\mathbf{T}}_r = \bar{\mathbf{T}}_r^T \mathbf{K}_g \bar{\mathbf{T}}_r. \tag{46}$$

Using Equations (44) and (46), Equation (42) is rewritten as

$$\xi_i \approx (\bar{\varphi}_p)_i^T [\bar{\lambda}_i \bar{\mathbf{T}}_0^T \mathbf{M}_g \bar{\mathbf{T}}_r + \bar{\lambda}_i^2 \bar{\mathbf{T}}_r^T \mathbf{M}_g \bar{\mathbf{T}}_r] (\bar{\varphi}_p)_i. \tag{47}$$

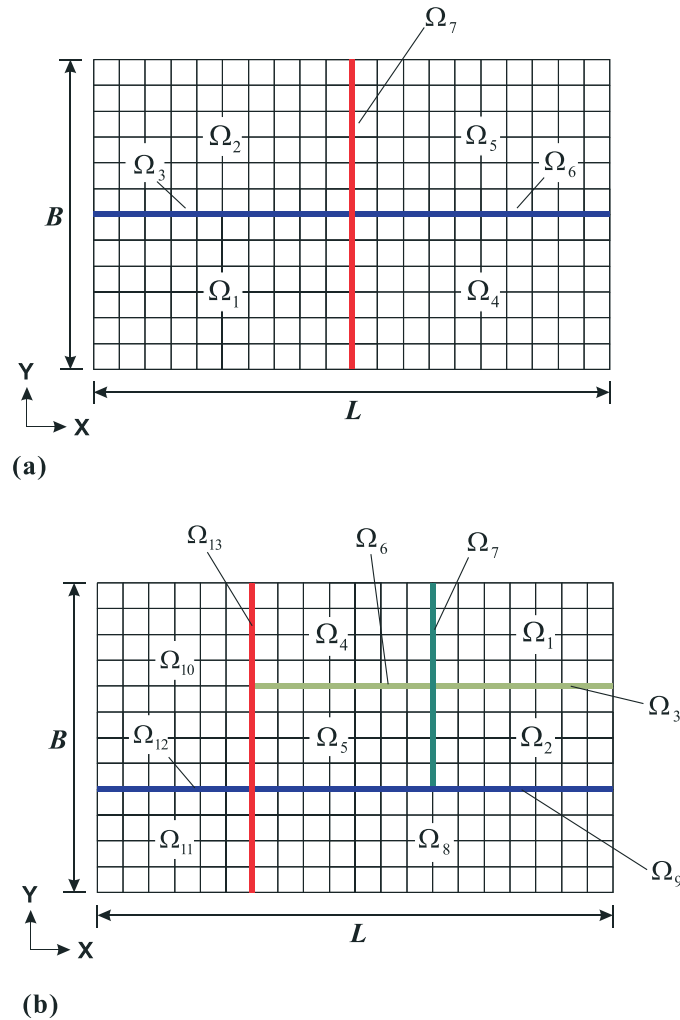


Figure 3. Rectangular plate problem: (a) partition type A and (b) partition type B.

In Equation (47), neglecting the second-order term of  $\bar{\lambda}_i$  and using Equation (43a), we can define an error estimator  $\mu_i$  as follows

$$\mu_i = \bar{\lambda}_i (\bar{\varphi}_p)_i^T \mathbf{A} \mathbf{F}_{rs} \mathbf{A}^T (\bar{\varphi}_p)_i \text{ with } \mathbf{A} = \Phi_d^T \tilde{\mathbf{M}}_g. \tag{48}$$

Note that  $\mathbf{A}$  can be calculated during the recursive transformation procedure of the mass matrix  $\mathbf{M}_g$  described in Equation (7).

In Equation 48, because of the symmetry of  $\mathbf{F}_{rs}$  matrix, it can be decomposed into three parts

$$\mathbf{F}_{rs} = \mathbf{F}_d + \mathbf{F}_u + \mathbf{F}_u^T, \tag{49}$$

in which  $\mathbf{F}_d$  and  $\mathbf{F}_u$  are the diagonal and upper triangular parts of  $\mathbf{F}_{rs}$ , respectively.

Substituting Equation (49) into Equation (48), the error estimator  $\mu_i$  for the  $i^{\text{th}}$  relative eigenvalue error is redefined as

$$\mu_i = \bar{\lambda}_i (\bar{\varphi}_p)_i^T \mathbf{E} (\bar{\varphi}_p)_i, \quad \mathbf{E} = \mathbf{E}_1 + \mathbf{E}_2 + \mathbf{E}_2^T \text{ with } \mathbf{E}_1 = \mathbf{A} \mathbf{F}_d \mathbf{A}^T, \mathbf{E}_2 = \mathbf{A} \mathbf{F}_u \mathbf{A}^T, \tag{50}$$

Table I. Retained substructural mode numbers  $N_i^d$  for the rectangular plate problem with partition type A.

Substructural level	Substructural number	$N_i^d$	Case 1	Case 2
Level 1	3	$N_3^d$	3	5
	6	$N_6^d$	3	5
Level 2	1	$N_1^d$	6	10
	2	$N_2^d$	6	10
	4	$N_4^d$	6	10
	5	$N_5^d$	6	10
		$N_d$	30	50

Level 0 is not listed here.

Table II. Retained substructural mode numbers  $N_i^d$  for the rectangular plate problem with partition type B.

Substructural level	Substructural number	$N_i^d$	Case 1	Case 2
Level 1	9	$N_9^d$	10	13
	12	$N_{12}^d$	4	5
Level 2	7	$N_7^d$	5	7
	8	$N_8^d$	9	12
	10	$N_{10}^d$	6	10
	11	$N_{11}^d$	3	5
Level 3	3	$N_3^d$	5	5
	6	$N_6^d$	3	3
Level 4	1	$N_1^d$	4	6
	2	$N_2^d$	2	3
	4	$N_4^d$	3	4
	5	$N_5^d$	1	2
		$N_d$	55	75

Level 0 is not listed here.

where  $\mathbf{E}$ ,  $\mathbf{E}_1$ , and  $\mathbf{E}_2$  are  $\bar{N}_p \times \bar{N}_p$  matrices. Therefore, we do not need to handle the matrices of global DOF size.

Here,  $\mathbf{E}_1$  and  $\mathbf{E}_2$  in Equation (50) can be expressed in a substructural component matrix form as follows

$$\mathbf{E}_{i,j}^1 = \sum_{k=1}^{N_S} \mathbf{A}_{i,k} \mathbf{F}_k^d \mathbf{A}_{k,j}^T, \quad \mathbf{E}_{i,j}^2 = \sum_{k=1}^{N_S} \mathbf{A}_{i,k} \mathbf{F}_k^u \mathbf{A}_{k,j}^T \text{ for } i, j = 1, 2, \dots, N_S \quad (51)$$

in which subscripts  $i$ ,  $j$ , and  $k$  denote the  $i^{\text{th}}$ ,  $j^{\text{th}}$ , and  $k^{\text{th}}$  substructural quantities, respectively. Thus,  $\mathbf{E}$  in Equation (50) can be efficiently calculated through Equation (51).

In reduced models, lower modes are more accurately approximated than higher modes. For this reason, we can expect that, in general, the error estimation accuracy is better in lower modes. We also note that the proposed error estimator  $\mu_i$  is not an upper or lower bound for the exact relative eigenvalue error  $\xi_i$ . Further studies are necessary to obtain a guaranteed upper bound.

It is possible to expect that the computational cost of the proposed error estimation method is not high because it only requires to calculate  $\mathbf{F}_{rs}$ ,  $\mathbf{A}$ , and  $\mathbf{E}$  matrices. The detailed computational cost breakdown is presented in Section 6.

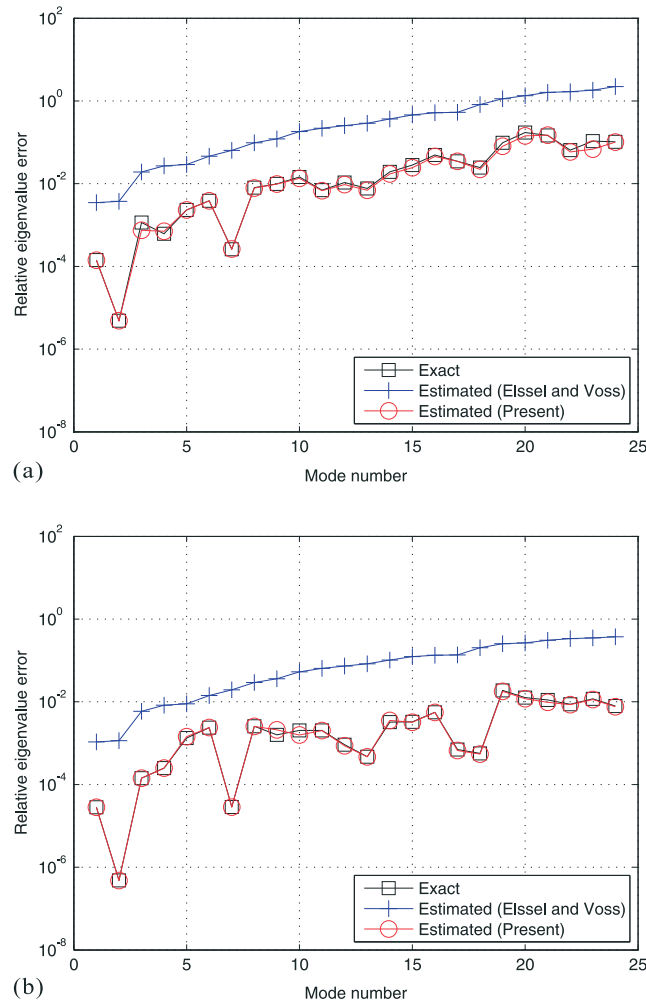


Figure 4. Exact and estimated relative eigenvalue errors for the rectangular plate problem with partition type A: (a)  $N_d = 30$  and (b)  $N_d = 50$ .

It is important to note that in this study, we only focused on the model reduction error. That is, the discretization error in original FE models was not considered, because the discretization error and its estimation methods have been well studied [25–27].

5. NUMERICAL EXAMPLES

In order to evaluate the performance and the computational efficiency of the proposed method, we here provide solutions to five numerical problems: rectangular plate, cylindrical solid, bench corner structure, turbine blade, and stiffened plate problems. For finite element modeling, the four-node Mixed Interpolation of Tensorial Components (MITC) shell (e.g., References [28–33]) and eight-node brick elements are used. The frequency cut-off method is employed to select the dominant substructural modes [7].

The relative eigenvalue errors estimated by the proposed error estimation method are compared with the exact relative eigenvalue errors. Furthermore, the estimated relative eigenvalue errors are also compared with those calculated by the previous error estimation method developed by Elssel and Voss [19],

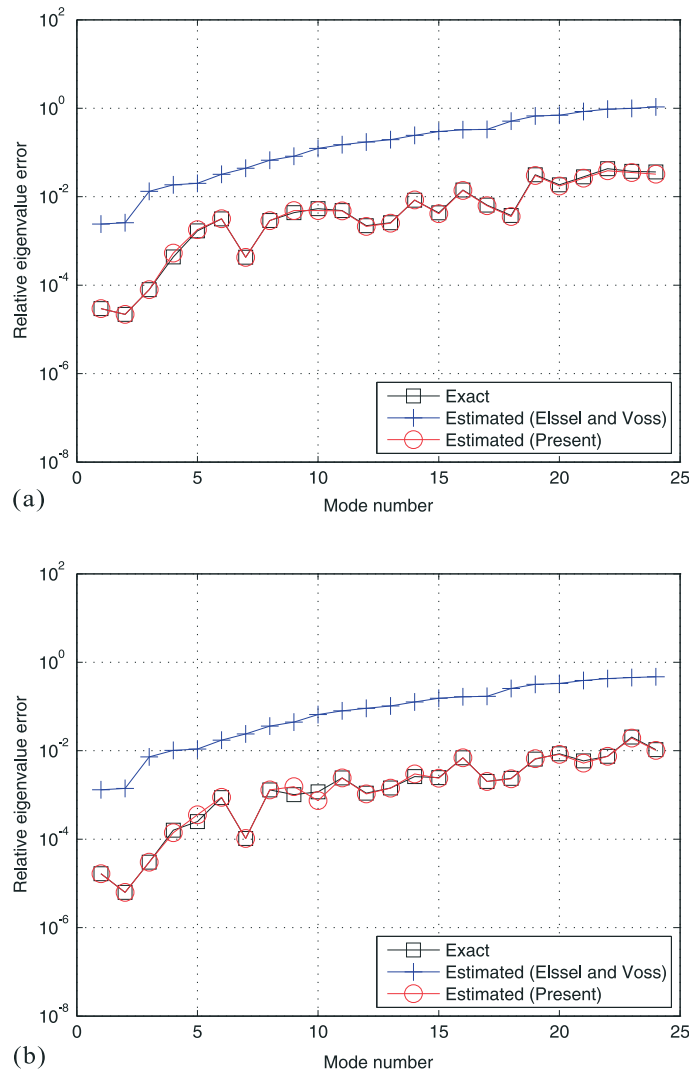


Figure 5. Exact and estimated relative eigenvalue errors for the rectangular plate problem with partition type B: (a)  $N_d = 55$  and (b)  $N_d = 75$ .

$$\hat{\mu}_i = \prod_{k=0}^p \left( 1 + \frac{\bar{\lambda}_i}{\lambda_k - \bar{\lambda}_i} \right) - 1, \quad (52)$$

where  $\lambda_k$  is the smallest residual eigenvalue on level  $k$  and  $p$  denotes the number of substructural level. The advantage of this error estimation method is the fact that almost no computational cost is required.

### 5.1. Rectangular plate problem

A rectangular plate shown in Figure 3 is considered. Length  $L$  is 20.0 m, width  $B$  is 12.0 m, and thickness  $h$  is 0.08 m. Young's modulus  $E$  is 206 GPa, Poisson's ratio  $\nu$  is 0.33, density  $\rho$  is 7850 kg/m<sup>3</sup>, and no boundary condition is imposed.

The plate structure is modeled by  $20 \times 12$  meshes of the four-node MITC shell finite elements and the number of total DOFs used is 1365. We consider two different partition types in Figure 3(a) and (b):

- Partition type A: The global structure is partitioned into seven substructures and three substructural levels (levels 0, 1, and 2); Figure 3(a). Retaining 30 and 50 substructural modes ( $N_d = 30$  and  $N_d = 50$ ), two numerical cases are considered.
- Partition type B: As shown in Figure 3(b), the number of substructures is 13 and the number of substructural levels is five (levels 0, 1, 2, 3, and 4). We retain 55 and 75 substructural modes for two numerical cases ( $N_d = 55$  and  $N_d = 75$ ).

The numbers of retained substructural modes  $N_i^d$  in both partition types are listed in Tables I and II.

Figures 4 and 5 show the exact and estimated relative eigenvalue errors in the partition types A and B, respectively. It is observed that the proposed error estimation method outperforms the previous method by Elssel and Voss [19]. The proposed error estimation method very accurately estimates the

Table III. Exact and estimated eigenvalue errors in the rectangular plate problem in Figure 3(a).

Mode number	Exact	Estimated (Elssel and Voss)	Estimated (Present)
1	1.42398E-04	3.47402E-03	1.41198E-04
2	4.84836E-06	3.72228E-03	4.84277E-06
3	1.14861E-03	1.91922E-02	7.45688E-04
4	6.15067E-04	2.69247E-02	7.05708E-04
5	2.32190E-03	2.90519E-02	2.31991E-03
6	3.84152E-03	4.62201E-02	3.84068E-03
7	2.59851E-04	6.38626E-02	2.64026E-04
8	7.99567E-03	9.70397E-02	7.83034E-03
9	9.85326E-03	1.20514E-01	9.80659E-03
10	1.44761E-02	1.81358E-01	1.34670E-02
11	6.99459E-03	2.19472E-01	6.78935E-03
12	1.06231E-02	2.54143E-01	9.48957E-03
13	7.65496E-03	2.88715E-01	6.92046E-03
14	1.93441E-02	3.66750E-01	1.71415E-02
15	2.81629E-02	4.58426E-01	2.43915E-02
16	4.95217E-02	5.18720E-01	4.54262E-02
17	3.45418E-02	5.32115E-01	3.46392E-02
18	2.44904E-02	8.20276E-01	2.20948E-02
19	9.76902E-02	1.13291E+00	8.02794E-02
20	1.72710E-01	1.33925E+00	1.43464E-01
21	1.47041E-01	1.61401E+00	1.48564E-01
22	6.47085E-02	1.67060E+00	5.87691E-02
23	1.06602E-01	1.82959E+00	6.84897E-02
24	1.02452E-01	2.22575E+00	1.01068E-01

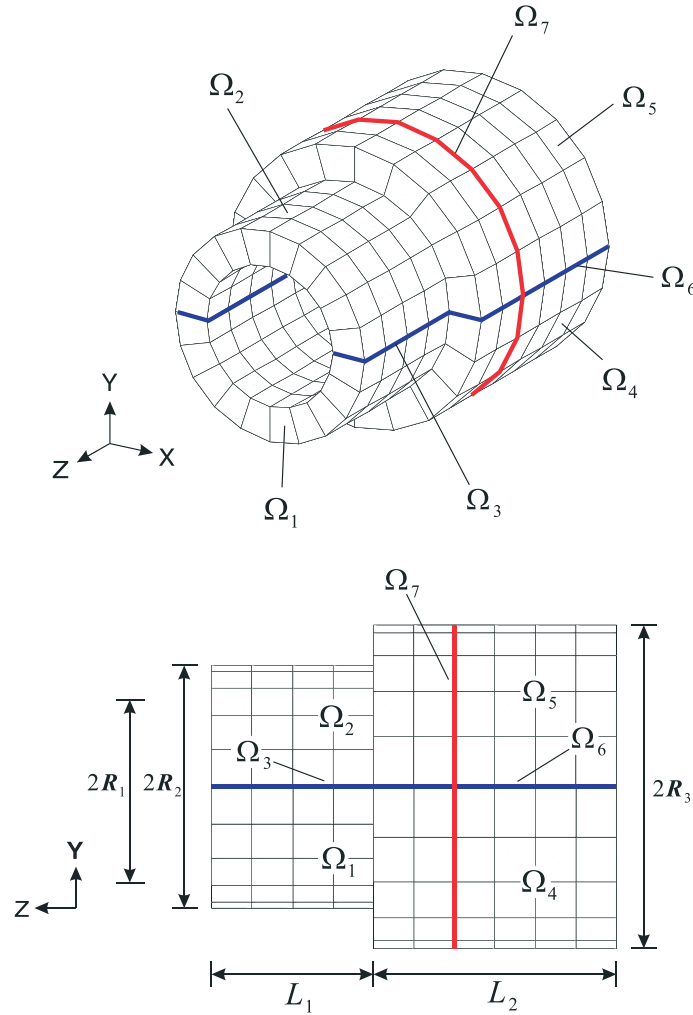


Figure 6. Cylindrical solid problem.

Table IV. Retained substructural mode numbers  $N_i^d$  for the cylindrical solid problem.

Substructural level	Substructural number	$N_i^d$	Case 1	Case 2
Level 1	3	$N_3^d$	12	20
	6	$N_6^d$	10	12
Level 2	1	$N_1^d$	13	26
	2	$N_2^d$	13	26
	4	$N_4^d$	11	18
	5	$N_5^d$	11	18
			$N_d$	70

Level 0 is not listed here.

relative eigenvalue errors in the reduced FE models. Table III lists the exact and estimated relative eigenvalue errors, corresponding to Figure 3(a). It is observed that the present error estimator  $\mu_i$  provides slightly larger (upper) values for the exact relative eigenvalue error  $\xi_i$ , except for 4th, 7th, 17th, and 21st modes, in the numerical cases considered. As mentioned in the previous section, the proposed error estimation method gives more accurate error estimations for lower modes.

### 5.2. Cylindrical solid problem

Let us consider a cylindrical solid problem with free boundary at both ends as shown in Figure 6. Lengths  $L_1$  and  $L_2$  are 0.16 and 0.24 m, respectively, and the radii  $R_1$ ,  $R_2$ , and  $R_3$  are 0.08, 0.12, and 0.16 m, respectively. Young's modulus  $E$  is 76 GPa, Poisson's ratio  $\nu$  is 0.33, density  $\rho$  is  $2796 \text{ kg/m}^3$ .

The cylindrical structure is modeled using eight-node brick elements, and the number of total DOFs used is 1740. As shown in Figure 6, the global structure is partitioned into seven substructures, and the number of substructural levels is three (levels 0, 1, and 2). Two different numbers of retained substructural modes ( $N_d = 70$  and  $N_d = 120$ ) are considered, as listed in Table IV.

Figure 7 shows the exact and estimated relative eigenvalue errors in the two numerical cases. It is observed that the performance of the present error estimation method is much more accurate than the error estimation method by Elssel and Voss [19]. For lower modes, the estimated relative eigenvalue errors are more accurate.

### 5.3. Bench corner structure problem

A bench corner structure in container ships is considered. This structure is a critical part with a high risk of fatigue cracking caused by structural vibration in ships. Lengths  $L_1$  and  $L_2$  are 4.0 and

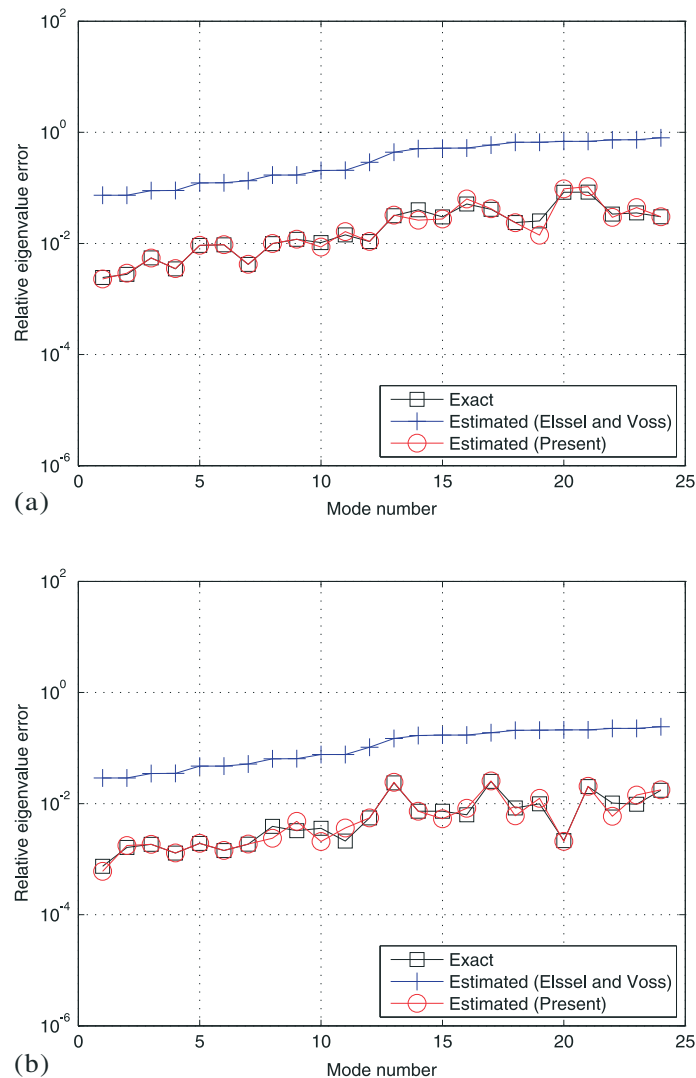


Figure 7. Exact and estimated relative eigenvalue errors for the cylindrical solid problem: (a)  $N_d = 70$  and (b)  $N_d = 120$ .

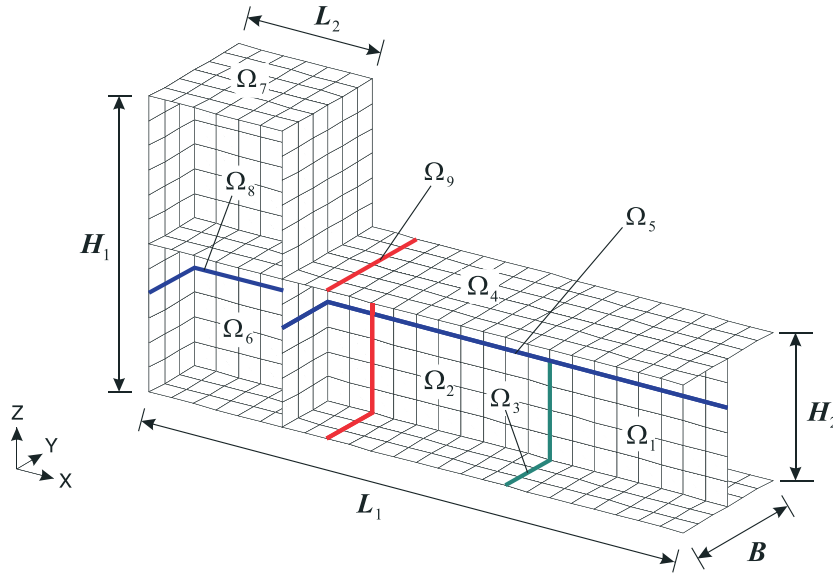


Figure 8. Bench corner structure problem.

Table V. Retained substructural mode numbers  $N_i^d$  for the bench corner structure problem.

Substructural level	Substructural number	$N_i^d$	Case 1	Case 2
Level 1	5	$N_5^d$	7	11
	8	$N_8^d$	8	10
Level 2	3	$N_3^d$	5	6
	4	$N_4^d$	11	14
	6	$N_6^d$	2	7
	7	$N_7^d$	11	18
Level 3	1	$N_1^d$	4	9
	2	$N_2^d$	2	5
		$N_d$	50	80

Level 0 is not listed here.

1.0 m, and heights  $H_1$  and  $H_2$  are 2.0 and 1.0 m. Width  $B$  is 1.0 m, and thickness  $h$  is 0.025 m. Young's modulus  $E$  is 210 GPa, Poisson's ratio  $\nu$  is 0.30, and density  $\rho$  is  $7850 \text{ kg/m}^3$ .

For finite element modeling, the four-node MITC shell finite elements (FEs) are used, and 3508 DOFs are considered for this problem. The FE model is partitioned into nine substructures with four substructural levels (levels 0, 1, 2, and 3), as shown in Figure 8. We retain 50 and 80 dominant substructural modes ( $N_d = 50$  and  $N_d = 80$ ), and in the two numerical cases, the numbers of dominant substructural modes  $N_i^d$  contained in the reduced FE models are listed in Table V. The exact and estimated relative eigenvalue errors are plotted in Figure 9. The present error estimation method consistently provides a very accurate estimation of the relative eigenvalue errors.

#### 5.4. Turbine blade problem

Here, we consider a turbine blade problem as shown in Figure 10. The turbine blade is fully fixed at  $x = 0$ . Length and thickness are 35 m and 0.05 m, respectively, Young's modulus  $E$  is 210 GPa, Poisson's ratio  $\nu$  is 0.3, and density  $\rho$  is  $7800 \text{ kg/m}^3$ . The detailed geometry has been described

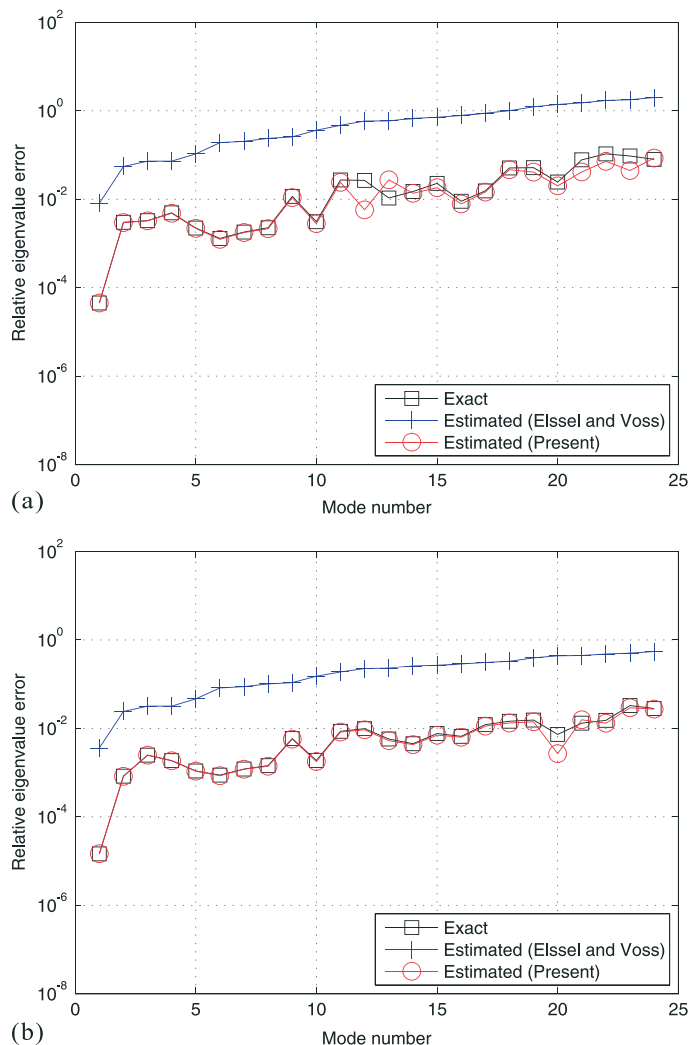


Figure 9. Exact and estimated relative eigenvalue errors for the bench corner structure problem: (a)  $N_d = 50$  and (b)  $N_d = 80$ .

[34]. We use 10300 shell finite elements and 10100 nodes (51308 DOFs). The global structure is partitioned into 19 substructures, and we here consider three substructural levels (0, 1, and 2) (Figure 10).

Two different numbers of retained substructural modes ( $N_d = 300$  and  $N_d = 500$ ) are considered, and the numbers of dominant substructural modes  $N_i^d$  contained in the reduced FE models are listed in Table VI. Figure 11 shows that the present error estimation method very accurately estimates the relative eigenvalue errors. As expected, the accuracy of the error estimation method is better in lower modes.

5.5. Stiffened plate problem

As shown in Figure 12, a stiffened plate, an important structural unit of ships, is considered. Length  $L$  and breadth  $B$  are 78.0 m and 44.0 m, respectively, and the stiffener spacing is 2.0 m. The stiffener is composed of a vertical web of height 0.05 m and a flange of breadth 0.02 m, and the thickness is 0.019 m. Young's modulus  $E$ , Poisson's ratio  $\nu$  and density  $\rho$  are 206 GPa, 0.3, and  $7850 \text{ kg/m}^3$ , respectively.

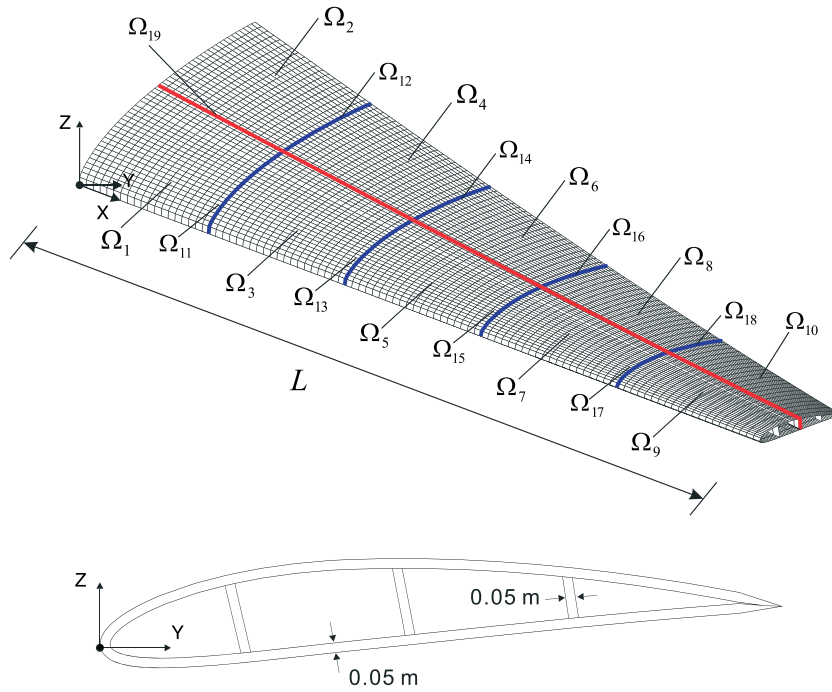


Figure 10. Turbine blade problem.

Table VI. Retained substructural mode numbers  $N_i^d$  for the turbine blade problem.

Substructural level	Substructural number	$N_i^d$	Case 1	Case 2
Level 1	11	$N_{11}^d$	3	3
	12	$N_{12}^d$	3	3
	13	$N_{13}^d$	3	3
	14	$N_{14}^d$	3	3
	15	$N_{15}^d$	3	3
	16	$N_{16}^d$	3	3
	17	$N_{17}^d$	3	3
	18	$N_{18}^d$	3	3
Level 2	1	$N_1^d$	29	49
	2	$N_2^d$	38	66
	3	$N_3^d$	35	63
	4	$N_4^d$	33	56
	5	$N_5^d$	32	52
	6	$N_6^d$	30	47
	7	$N_7^d$	26	42
	8	$N_8^d$	22	37
	9	$N_9^d$	17	36
	10	$N_{10}^d$	14	28
		$N_d$	300	500

Level 0 is not listed here.

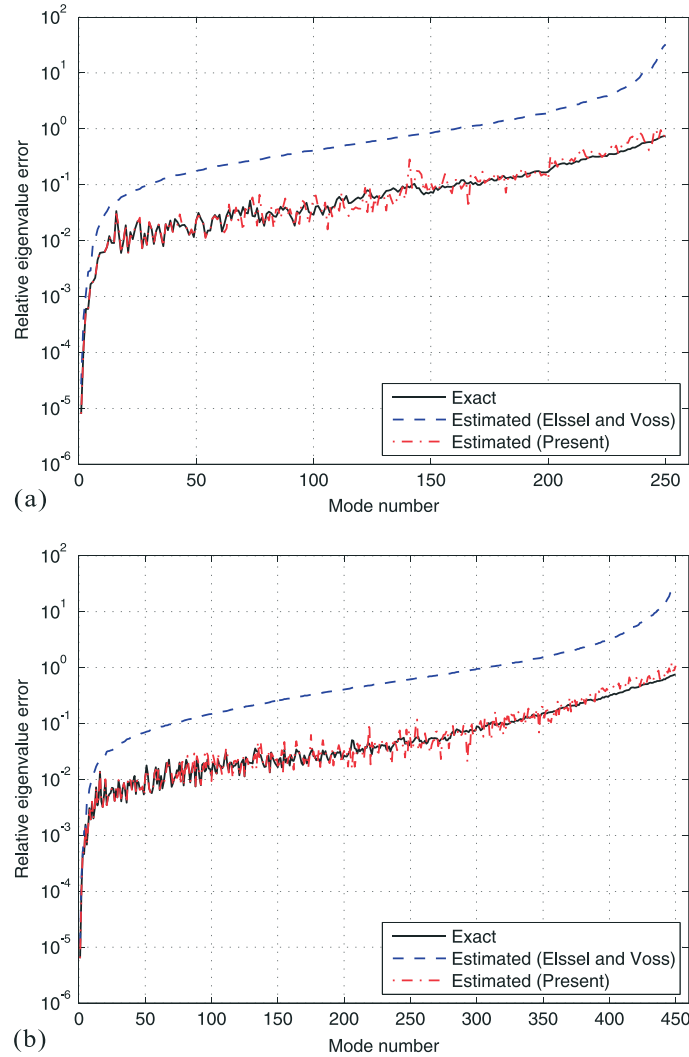


Figure 11. Exact and estimated relative eigenvalue errors for the turbine blade problem: (a)  $N_d = 300$  and (b)  $N_d = 500$ .

The number of DOFs is 1004088, and the global structure is automatically partitioned into 1023 substructures with 10 substructural levels using METIS [35], which is an efficient mesh partitioning software package. For two numerical cases, we use 2200 and 5450 dominant substructural modes ( $N_d = 2200$  and  $N_d = 5450$ ). The exact and estimated relative eigenvalue errors are plotted in Figure 13 for the two numerical cases. This clearly shows the accuracy of the proposed error estimator.

## 6. COMPUTATIONAL COST

In this work, a sparse matrix computation with MATLAB (MathWorks, Natick, MA, USA) is used in a personal computer (Intel core (TM) i7-3770, 3.40 GHz CPU, 32 GB RAM). To investigate the computational cost for the proposed error estimator  $\mu_i$  in Equation (50), we calculate the computational cost breakdown for  $\mathbf{F}_{rs}$ ,  $\mathbf{A}$ , and  $\mathbf{E}$  matrices.

In the turbine blade problem, we investigate the computational cost required for the proposed error estimator. Table VII lists the breakdown of computational cost for estimating relative eigenvalue errors of 250 modes in the turbine blade problem ( $N_d = 300$ ) The results show that compared with

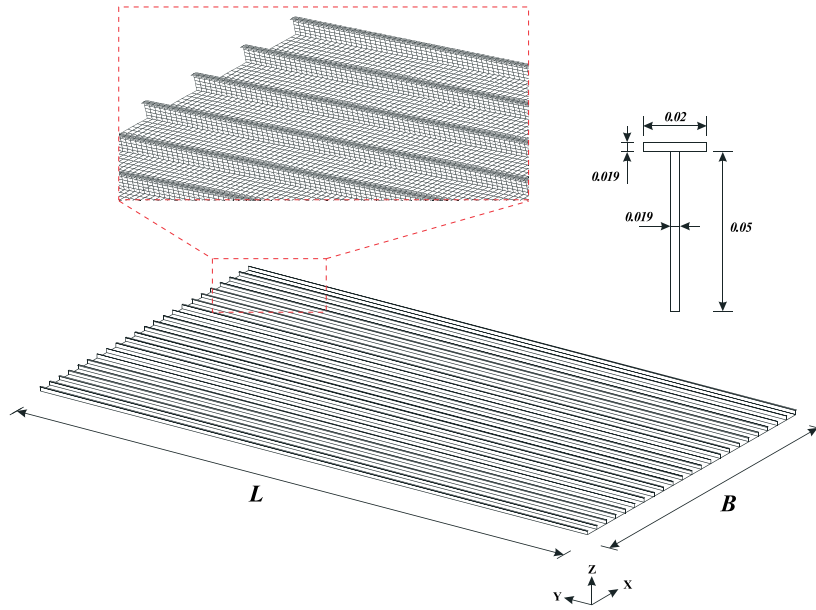


Figure 12. Stiffened plate problem.

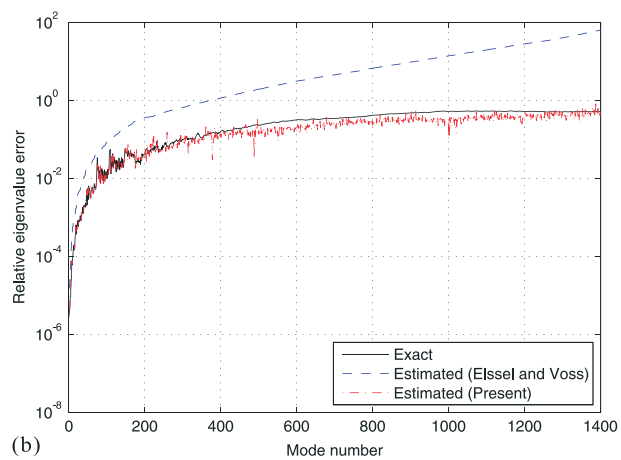
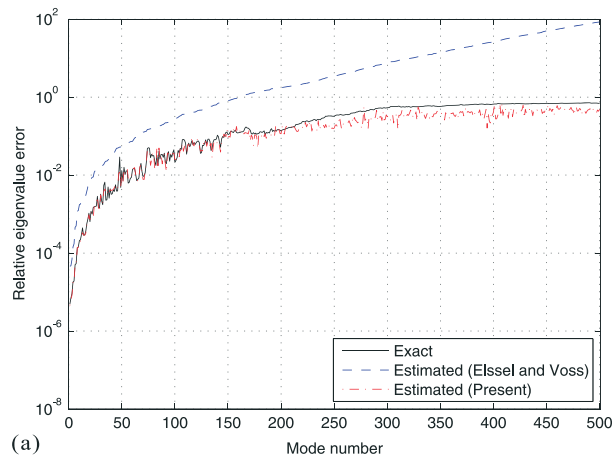


Figure 13. Exact and estimated relative eigenvalue errors for the stiffened plate problem: (a)  $N_d = 2200$  and (b)  $N_d = 5450$ .

the computation time of the AMLS method, 7.91% of additional computation time is required to calculate the relative eigenvalue errors in 250 global modes

Table VIII shows the details of computational cost when  $N_d = 5450$  for the stiffened plate problem. Compared with the computation time required for the AMLS method, the present error estimation method requires 7.77% of additional computation time to calculate the relative eigenvalue errors of 1400 global modes

We here present the computational costs for the FE models with 51308 and 1004088 DOFs. However, additional tests will be required to consider FE models with more than several millions of DOFs. For this work, much more effective implementations and high-performance computers will be necessary.

Here, we also compare the computational costs of the present and of the Elssel and Voss error estimation methods. Table IX presents normalized computation times for the relative eigenvalue errors in the five FE models considered in this study. The computation times are normalized by the total computation time of the AMLS method. Numerical results show that the present error estimation method is more expensive than the Elssel and Voss method. Note that the Elssel and Voss method is an a priori method, but the present method is an a posteriori method.

Table VII. Computational cost breakdown for the present error estimation method. Turbine blade problem,  $N_d = 300$ .

	Items	Related equations	Computation times	
			[sec]	Ratio [%]
AMLS	Transformation procedures	13	46.55	99.30
	Solution of the reduced eigenvalue problem	14	0.33	0.70
	Total	—	46.88	100.00
Error estimation	Calculation of the residual flexibility matrix $\mathbf{F}_{r,s}$	36	0.55	1.17
	Construction of $\mathbf{A}$ and $\mathbf{E}$ matrices	48, 51	2.36	5.03
	Calculation error estimator $\mu_i$	50	0.80	1.71
	Total	—	3.71	7.91

Table VIII. Computational cost breakdown for the present error estimation method. Stiffened plate problem,  $N_d = 5450$ .

	Items	Related equations	Computation times	
			[sec]	Ratio [%]
AMLS	Transformation procedures	13	3355.02	96.74
	Solution of the reduced eigenvalue problem	14	113.21	3.26
	Total	—	3468.23	100.00
Error estimation	Calculation of the residual flexibility matrix $\mathbf{F}_{r,s}$	36	36.37	1.05
	Construction of $\mathbf{A}$ and $\mathbf{E}$ matrices	48, 51	227.31	6.55
	Calculation error estimator $\mu_i$	50	5.83	0.17
	Total	—	269.51	7.77

Table IX. Computational costs of the present and of the Elssel and Voss error estimation methods.

	The number of $\mu_i$ calculated	DOFs		Normalized computation time	
		$N_g$	$\bar{N}_p$	Elssel and Voss	Present
Rectangular plate ( $N_d = 30$ )	24	1365	215	0.001121	0.09107
Cylindrical solid ( $N_d = 70$ )	24	1740	250	0.000682	0.08974
Bench corner structure ( $N_d = 50$ )	24	3508	147	0.000297	0.03367
Turbine blade ( $N_d = 300$ )	250	51308	1500	0.000020	0.07911
Stiffened plate ( $N_d = 5450$ )	1400	1004088	7796	0.000001	0.07771

The computation times are normalized by the computation time of the AMLS method.

## 7. CONCLUSIONS

In this study, we proposed an error estimation method to accurately estimate the relative eigenvalue errors in structural FE models reduced by the AMLS method. To develop the error estimation method for the AMLS method, in this study, an enhanced transformation matrix was newly developed that considered the residual mode effect. This enhanced transformation matrix makes it possible to more accurately approximate the global eigenvectors. Using the enhanced transformation matrix, we then derived the error estimation method for the AMLS method.

The excellent performance of the proposed error estimation method was demonstrated through various numerical examples. The computational efficiency of the proposed method was also studied for the FE models considered in this study. In future work, it will be valuable to improve the computational efficiency of the error estimation method considering FE models with more than several millions of DOFs.

## ACKNOWLEDGEMENTS

This work was supported by the Basic Science Research Program through the National Research Foundation of Korea (NRF) funded by the Ministry of Education, Science and Technology (No. 2014R1A1A1A05007219), and the Human Resources Program in Energy Technology of the Korea Institute of Energy Technology Evaluation and Planning (KETEP), granted financial resource from the Ministry of Trade, Industry & Energy, Republic of Korea (No. 20134030200300).

## REFERENCES

1. Kim JG, Lee KH, Lee PS. Estimating relative eigenvalue errors in the Craig–Bampton method. *Computers and Structures* 2014; **139**:54–64.
2. Guyan R. Reduction of stiffness and mass matrices. *AIAA Journal* 1965; **3**(2):380.
3. Irons BM. Structural eigenvalue problems: elimination of unwanted variables. *AIAA Journal* 1965; **3**:961–962.
4. Kidder RL. Reduction of structural frequency equations. *AIAA Journal* 1973; **11**(6):892–892.
5. Kuhar EJ, Stahle CV. Dynamic transformation method for modal synthesis, *AIAA Journal*. Vol. 12, iss. 1974; **5**:672–678.
6. Kim JG, Lee PS. An accurate error estimator for Guyan reduction. *Computer Methods in Applied Mechanics and Engineering* 2014; **279**:1–19.
7. Hurty W. Dynamic analysis of structural systems using component modes. *AIAA Journal* 1965; **3**(4):678–685.
8. Craig RR, Bampton MCC. Coupling of substructures for dynamic analysis. *AIAA Journal* 1965; **6**(7):1313–1319.
9. MacNeal RH. Hybrid method of component mode synthesis. *Computers and Structures* 1971; **1**(4):581–601.

10. Benfield WA, Hruda RF. Vibration analysis of structures by component mode substitution. *AIAA Journal* 1971; **9**:1255–1261.
11. Rubin S. Improved component-mode representation for structural dynamic analysis. *AIAA Journal* 1975; **13**(8): 995–1006.
12. Park KC, Park YH. Partitioned component mode synthesis via a flexibility approach. *AIAA Journal* 2004; **42**(6):1236–1245.
13. Rixen DJ. A dual Craig–Bampton method for dynamic substructuring. *Journal of Computational and Applied Mathematics* 2004; **162**(1-2):383–391.
14. Bourquin F. Analysis and comparison of several component mode synthesis methods on one dimensional domains. *Numerische Mathematik* 1990; **1**:11–33.
15. Bourquin F. Component mode synthesis eigenvalues of second order operators: discretization and algorithm. *Mathematical Modelling and Numerical Analysis* 1992; **26**(3):385–423.
16. Bourquin F, d’Hennezel F. Intrinsic component mode synthesis and plate vibrations. *Computers and Structures* 1992; **44**:315–324. 1-2.
17. Bourquin F, d’Hennezel F. Numerical study of an intrinsic component mode synthesis method. *Computer Methods in Applied Mechanics and Engineering* 1992; **97**(1):49–76.
18. Bennighof JK, Lehoucq RB. An automated multi-level substructuring method for eigenspace computation in linear elastodynamics. *SIAM Journal on Scientific Computing* 2004; **25**(6):2084–2106.
19. Yang C, Gao W, Bai Z, Li XS, Lee LQ, Husbands P, Ng E. An algebraic substructuring method for large-scale eigenvalue calculation. *SIAM Journal on Scientific Computing* 2005; **27**:873–892.
20. Elssel K, Voss H. An a priori bound for automated multi-level substructuring. *SIAM Journal on Matrix Analysis and Applications* 2007; **2**:386–397.
21. Jakobsson H, Larson MG. A posteriori error analysis of component mode synthesis for the elliptic eigenvalue problem. *Computer Methods in Applied Mechanics and Engineering* 2011; **200**:2840–2847.
22. Park KC, Kim JG, Lee PS. A mode selection criterion based on flexibility approach in component mode synthesis. *Proceeding 53th AIAA/ASME/ASCE/AHS/ASC Structures, Structural Dynamics, and Materials Conference Hawaii, USA, 2012*.
23. Bennighof JK, Kaplan MF. Frequency sweep analysis using multi-level substructuring, global modes and iteration. *Proceedings of the 39th Annual AIAA Structural Dynamics and Materials Conference, Long Beach, Ca, 1998*.
24. Kaplan F. Implementation of automated multi-level substructuring for frequency response analysis of structures. *PhD thesis, Department of Aerospace Engineering & Engineering Mechanics, University of Texas at Austin, Austin TX, 2001*.
25. Babuška I, Rheinboldt WC. Error estimates for adaptive finite element computations. *SIAM Journal on Numerical Analysis* 1978; **15**(4):736–754.
26. Babuška I, Rheinboldt WC. A posteriori error estimates for the finite element method. *International Journal for Numerical Methods in Engineering* 1978; **12**(10):1597–1615.
27. Ladeveze P, Leguillon D. Error estimate procedure in the finite element method and applications. *SIAM Journal on Numerical Analysis* 1983; **20**(3):485–509.
28. Dvorkin EN, Bathe KJ. A continuum mechanics based four-node shell element for general nonlinear analysis. *Engineering Computations* 1984; **1**(1):77–88.
29. Bathe KJ, Dvorkin EN. A formulation of general shell elements—the use of mixed interpolation of tensorial components. *International Journal for Numerical Methods in Engineering* 1986; **22**(3):697–722.
30. Lee PS, Bathe KJ. Development of MITC isotropic triangular shell finite elements. *Computers and Structures* 2004; **82**(11-12):945–962.
31. Lee YG, Yoon KH, Lee PS. Improving the MITC3 shell finite element by using the Hellinger–Reissner principle. *Computers and Structures* 2012; **110–111**:93–106.
32. Jeon HM, Lee PS, Bathe KJ. The MITC3 shell finite element enriched by interpolation covers. *Computers and Structures* 2014; **134**:128–142.
33. Lee Y, Lee PS, Bathe KJ. The MITC3+ shell finite element and its performance. *Computers and Structures* 2014; **138**:12–23.
34. Yoon K, Lee YG, Lee PS. A continuum mechanics based 3-D beam finite element with warping displacements and its modeling capabilities. *Structural Engineering and Mechanics* 2012; **43**:411–437.
35. Karypis G, Kumar V. METIS v4.0, A software package for partitioning unstructured graphs, partitioning meshes, and computing fill-reducing orderings of sparse matrices. *Technical Report*, University of Minnesota: Minneapolis, MN, 1998.